

Modeling the ten-image lensed system B1933+503

S. Nair^{1,2} \star

¹*Kapteyn Astronomical Institute, P.O. Box 800, 9700 AV Groningen, The Netherlands*

²*University of Manchester, NRAL Jodrell Bank, Macclesfield, Cheshire SK11 9DL, United Kingdom*

March 7, 1998

ABSTRACT

A gravitational lens model is presented for the newly discovered 10-image system B1933+503. The underlying object, revealed by modeling, is a triple radio source on the scale of a couple of hundred mas that is well-aligned along the line of sight with a foreground and somewhat flattened lensing galaxy, whose orientation and location match that of an observed galaxy, known to be at a redshift of 0.755. Uncertainties in the modeling are obtained by a Monte Carlo exercise. Observational tests of the lens model are proposed, and the time delays between various pairs of images are determined as the core of the source is known to be significantly variable. Future observations of the lens hold the key to using B1933+503 to constrain Hubble’s Constant. Despite the absence of a source redshift, the system’s utility as a probe of the lens galaxy’s structure is unparalleled as it provides a surfeit of easily identifiable constraints for modeling the system.

Key words: gravitational lensing: individual systems: B1933+503 – galaxies:structure

1 INTRODUCTION

In a companion paper, Sykes et al. (1997) report the discovery of a spectacular arcsecond-scale gravitationally lensed radio system, B1933+503 (1934+504) in J2000 coordinates), which was found in the course of the Cosmic Lens All-Sky Survey (CLASS). CLASS is a search for radio sources that exhibit multiple components with flat radio spectral indices ($\alpha < 0.5$, with flux density $S_\nu \sim \nu^{-\alpha}$). Such systems are typically extragalactic, and result from gravitational multiple imaging of a background source such as a quasar or an AGN by a foreground galaxy lying along the line of sight to it. The first gravitational lens to be identified on the basis of its multiple flat-spectrum radio components was PKS1830–211, by Rao & Subrahmanyan (1988). A survey conducted from Jodrell Bank (Patnaik et al. 1992), now known as the Jodrell VLA Astrometric Survey or JVAS, employed this property as a highly successful filter for identifying new lensed systems: B0218+357 (Patnaik et al. 1993), B1422+231 (Patnaik et al. 1992), B1030+074 (King & Browne 1996 and Xanthopoulos et al. 1997) and B1938+666 (King et al. 1997a, King et al. 1997b), in addition to the promising candidate lensed system B2114+022 (Augusto et al. 1996). The ongoing CLASS project follows on from and contains JVAS, and together these have discovered more than 13 systems so far (inclusive of candidates yet to be confirmed) in a survey of nearly 8000 sources. Descriptions of this survey are to be found in Myers et al.(1995), Jackson et al. (1995,

\star Present address: Astrophysics Group, Raman Research Institute, C. V. Raman Avenue, Bangalore 560080, India.

1997b) and Browne et al. (1997). Newly established finds include B1608+656 (Myers et al. 1995, Fassnacht et al. 1996), B1600+434 (Jackson et al. 1995, Koopmans et al. 1997a), B0712+472 (Jackson et al. 1997a), B1933+503 (Sykes et al. 1997) and B1130+382 (Koopmans et al. 1997b).

B1933+503 bears a superficial resemblance to an Einstein Ring in its morphology, but is composed of at least 10 discrete components, as reported by Sykes et al. (1997). It has been investigated over the range of radio frequencies 1.7–15 GHz (VLA 5, 8.4 & 15 GHz, MERLIN 1.7 & 5 GHz and VLBA 1.7 & 5 GHz); only the MERLIN 1.7 GHz observations appear to have the combination of dynamic range and resolution required to pick up all 10 components. However, Sykes et al. (1997) provide sufficient observational evidence to note that (a) four of the components have similar, complex radio spectra peaking around 5 GHz and are compact, being a few mas in size, (b) of the remaining six, four have steep radio spectra over the range of frequencies observed, but appear to be fairly compact (also on the scale of a few mas). The remaining two components probably also have steep radio spectra. Sykes et al. (1997) also infer that the components which have complex radio spectra appear to be variable by as much as 33% at 15 GHz over the timescale of a couple of months. HST observations with WFPC2 succeed in picking up what appears to be a flattened galaxy located near the centre of the ring of radio components. This object has an I magnitude of 20.6 at 810 nm and is elongated at a position angle of -40 ± 5 degrees, with an axial ratio (b/a) in the plane of the sky of 0.45–0.55. At 540 nm, there is no sign of the galaxy down to V magnitude 22.5. An optical spectrum taken with the Keck telescope using the Low Resolution Imaging Spectrometer (LRIS) shows the presence of absorption and emission corresponding to a redshift of 0.755, which probably corresponds to the galaxy rather than the source since no optical counterparts of the images have been detected as yet (Sykes et al. 1997).

2 B1933+503: THE LENS INTERPRETATION

A galaxy acting as a lens typically produces five, three or a single image(s) of a background source, with increasing degree of misalignment of the source in the plane of the sky from the line of sight to the lens (see, e.g., Schneider, Ehlers & Falco 1992 for a review of the properties of gravitational lensing by galaxies). When five or three images are formed, one occurs very near the centre of the galaxy and suffers a high degree of demagnification, so observationally there would appear to be either four images (a quad) or two images (a double) of the source. Most radio sources discovered so far that are lensed by galaxies and exhibit multiple compact flat-spectrum features can be clearly classified as either quad or double systems. B1938+666 (King et al. 1997) has two components in the background source, one of which is quadruply imaged while the other is a double. With its 10 features, B1933+503 is thus simplest understood as a triple radio source, the individual components of which have been multiply imaged into a quad, a quad and a double.

The MERLIN 1.7 GHz map of Sykes et al. (1997) (at top left in fig.1 of that paper) is the starting point of the present modeling exercise. Most of the components in this map can be grouped into one or the other of two quad con-

figurations. The first quad involves features 2, 5 and 7. The elongated morphology of feature 2 may be interpreted as a pair of images that are partially merged across the tangential critical curve (see Fig. 1(a)). There appear to be two strong peaks of flux density in feature 2 in the 1.7 GHz map of Sykes et al. (1997), and these will be referred to as 2a (east) and 2b (west) in the present work. The second quad is formed by components 1, 3, 4 and 6. Component 8, lying as it does within the circle of images, cannot then be singly imaged; its counterpart image is to be found in the faint feature 1a to the NE of component 1.

The two-image configuration formed by 1a and 8 is unusual in that 8 is so bright by comparison to 1a, despite its being nearer to the lens centre. This provides an interesting constraint on the lens model, since this relatively rare configuration can be obtained if image 8 is derived from three images that have just barely merged with each other into a single bright image. The source that is imaged into 1a and 8 must lie just outside a cusp of the tangential caustic in the source plane, but within the radial caustic. (This is illustrated in Fig. 1(b), a result from the lens modeling described in Sects. 3 and 4).

Within this picture, the underlying source prior to imaging by the lens would consist of a central radio core which shares the spectral and morphological properties of images 1, 3, 4, and 6, and is thus flat-spectrum and compact. The radio core is flanked by two steeper spectrum radio features, the trio being found by actual modeling to lie almost in a straight line, on the scale of a couple of hundred mas (Fig. 1(b)).

In principle, an alternative classification of the images could group 2 (seen again as a pair of images), 7, and 4 together, and 1, 3, 6, and 8 into a second quad. This would require 5 to be singly-imaged, as also 1a, unless each of them is an element of a double with a counterpart image within the circle of images which is too weak to be mapped. We can discard this and related scenarios in view of the support that the earlier classification receives from the radio spectra in figure 2 of Sykes et al. 1997, the VLBA 5GHz map in figure 1 (Sykes et al. 1997), and the pattern of variability discussed in that paper. (Amusingly, the image classification described earlier was worked out prior to any knowledge of the radio spectra or the VLBA observations.)

3 LENS MODELING

A modeling code has been developed that seeks a best-fit model for B1933+503, following the methods of Kayser & Schramm (1988) and Kochanek (1991). These employ a penalty function, which is minimised over the parameter space of a parametrized lens mass model, to yield a ‘best fit’ lens. Although the observed flattening of the lens suggests that it could be a disk galaxy which would typically consist of a disk, a spheroid and a halo, it is treated here as a single component elliptical lens approximating the overall mass distribution. The lensing galaxy is described by a non-singular isothermal ellipsoidal mass profile (the ‘PIEMD’ of Kassiola & Kovner 1993). The mass density distribution in the lens, ρ , follows the form:

$$\rho(m) = \rho_o / (1 + (m/a)^2), \quad (1)$$

where a is the scale length of the mass distribution, ρ_o is the central mass density, and $m^2 = x^2 + y^2/(1 - e^2) + z^2$ is the semi-major axis of an ellipsoidal shell of constant mass density. The lens is thus an oblate spheroid with axial ratio given by $\sqrt{1 - e^2}$, and is assumed to be viewed edge-on. (The x - and y - axes are confined to the plane of the sky, the orientation being set by modeling the lensed system; in the absence of concrete information about the nature of the lens, this model approximates the behaviour of either an elliptical or a spiral galaxy). The lens model has six parameters, these being the coordinates of the lens centre in the lens plane, a mass parameter describing the strength of the lens, its scale length, ellipticity and orientation in the plane of the sky. The mass parameter, σ_m , is related to the central density and the scale length: $\rho_o = 9\sigma_m^2/4\pi Ga^2$.

The complex scattering function formalism of Bourassa, Kantowski & Norton (1973) and Bourassa & Kantowski (1975) is employed, which permits analytical expressions to be obtained for the lensing action of a spheroidal mass distribution. In this formalism, the lens equation relating the source position in the plane of the sky, $\mathbf{z}_s = x_s + iy_s$, to that of its images, $\mathbf{z}_i = x + iy$, via a scattering function, $\mathbf{I}(x, y)$, is given by:

$$\mathbf{z}_s = \mathbf{z}_i - \frac{4GF_d}{c^2} \mathbf{I}^* \quad (2).$$

\mathbf{I}^* denotes the complex conjugate of the scattering function, which is proportional to σ_m^2 . \mathbf{I}^* is a function of image position \mathbf{z}_i as well as of the lens parameters \mathbf{p}_j . G is the gravitational constant, and F_d is the ratio of two angular diameter distances, that between lens and source, D_{ls} , and that between observer and source, D_s (since the redshift of the source is unknown at present, F_d is absorbed into the lens parameter σ_m^2 and the image and source positions are in angular units in the plane of the sky). The scattering function for the density profile in Eqn.(1) is given by expression (4.1.2) of Kassiola & Kovner (1993).

3.1 Constraints on the Modeling

Details of the image positions, relative to an initial guess lens centre, are listed in Table 1, in which the images are grouped according to their membership of a particular image configuration. Each multiple image configuration of N images provides $2(N-1)$ positional constraints (eliminating the common source position between pairs of images in a group; see Eqn.(2)). Thus, the two quads and the double image configuration of B1933+503 supply a maximum of $6+6+2=14$ constraints. This surfeit of constraints over parameters permits the luxury of ignoring the relatively uncertain positions of images 2a and 2b: these images straddle the tangential critical curve and each should theoretically be significantly brighter than either 5 or 7, which share the same source but are removed from any critical curves. This source, being of steep radio spectrum, is presumably non-variable (note the constancy of the flux ratio for images 7 and 5 in Table 1; the observations have been taken at different epochs). However, from table 2 of Sykes et al. (1997) it is apparent that in almost every observation, the *combined* flux density of 2a and 2b is lower than that of 5 or 7. One is led to conclude that the source of the image set (2a, 2b, 5, 7) is extended and is only partially imaged in the vicinity of

the tangential critical curve. Thus both the positions of 2a and 2b and their flux densities are undependable inputs to the modeling. Nevertheless, the fact that the image parities must be reversed between the positions of features 2a and 2b (see Table 2) proves very useful in constraining the location of the tangential critical curve during the modeling process, and this parity information is usable. Thus, only $2+6+2=10$ *positional* constraints are actually employed.

Ratios between the observed flux densities of pairs of images in a particular configuration generally provide an effective set of constraints on the modeling. However, if the source shows temporal variations in flux density, such changes manifest at different times in the various images owing to differential time delays in the arrival time at the observer for light from them. In B1933+503, it is known that the quad images (1, 3, 4, 6), arising from the flat-spectrum core, are significantly variable as discussed in Section 1. Hence constraints derived from their flux densities at a given epoch of observation could be uncertain by as much as 40% in the higher frequency observations. Accordingly, these are not be used in the present modeling exercise. Of the quad (2a, 2b, 5, 7), flux density ratios involving 2a and 2b are neglected, as described earlier, but the ratio for image 7 to image 5 appears to be robust (see Table 1); the source is of steep-spectrum and is not expected to be variable. Similarly, the flux density ratio of image 8 to 1a should be non-variable, but in practice this is affected particularly by the uncertainty in 1a, on account of its faintness. No flux density ratio constraints are actually employed in the modeling, but a good model may reasonably be expected to reproduce the ratios 7/5 and 8/1a.

In the absence of reliable image flux density ratios, the image *parities* provide important constraints on the modeling. The parity $(-1)^n$ for an image in a given configuration (quad or double) represents how the source maps onto that image, n being the number of reflections that it experiences about a set of coordinate axes centred on the image (for a single lens plane, no rotations occur). The theoretically expected image parities can be easily worked out by inspection for standard elliptical lenses (see Blandford & Narayan 1986, for example), and are listed in Table 2 for B1933+503. This set of constraints essentially determines the lens orientation in the plane of the sky.

3.2 The Penalty Function

For the desired lens model, the positions of those images belonging to the same quad or double configuration must map back through the lens, via the lens equation, to their shared source position. The penalty function to be minimised is obtained in the following manner : In general, having guessed an initial set of lens parameters, image positions corresponding to the same quad or double do not map back via Eqn.(2) to the same source position. A summed squared mismatch between the various source positions obtained by backprojecting the observed image positions, taken pairwise and divided by the number of images involved, forms the first part of the penalty function; this should ideally be as small as possible for each set of quads and the double. In the literature, it has been popular to multiply the errors in source recovery (departures from the average recovered source position) by the model magnifications of each image, converting

these errors to values that can be compared directly with the observational errors (e.g. Kochanek 1991). The minimization of the error function is then carried out in the image plane. In the present work, we have avoided using the model magnifications to bias the penalty function. This is with good reason: trials in which it was attempted to minimize the mismatch in the image plane after multiplying the source plane mismatches with the local image magnifications tended to locate models with enormously high image magnifications ($\sim 10^4$ and greater). In fact, given the freedom that a mass model with a finite scale length permits, the program tended to place the tangential critical curve as close to the images as it could (by centering the lens with respect to the images and making it as round as possible). Trying to minimize the *source plane* mismatch appears to be free of this bias and the results accord with trials with synthetic data from (known) lens models, obtained using a root-finding algorithm to solve the lens equation for the image positions corresponding to a given source.

The second part of the penalty function incorporates the image parity constraints. Only those lens models are accepted which exactly match the predicted pattern of image parities. This ensures that unphysical configurations are not selected by the program. Accordingly, the penalty associated with a parity mismatch is very high. The penalty function reads as:

$$\phi = \sum_{N_k=1}^3 \left(\frac{1}{N_k} \sum_{i<j}^{N_k} |z_{s,i} - z_{s,j}|^2 / \sigma^2 + \sum_{m=1}^{N_k} 10^4 \Gamma(P_m P_{em}) \right), \quad (3)$$

where N_k denotes the number of images in the image group (quad or double), σ is the tolerance in recovering the source position, and P_m and P_{em} are the model and expected values of parity for image n in a given group. The parities take values of either +1 or -1. $\Gamma(P_m P_{em})$ is a function with value zero for $P_m P_{em} > 0$, else it is unity. The large penalty associated with this part of the function ϕ ensures that parity match is obtained almost at the outset of the minimization process.

Minimization of the penalty function is achieved using a program, 'simann.f', written by Goffe (based on Goffe et al. 1994, and available from the NETLIB public access site on the Internet at the location <http://www.netlib.org/opt/simann.f>). This program employs the method of simulated annealing for optimization. It is found to be particularly useful in accomodating the sudden discontinuities that arise in the penalty function, accompanying changes in the model values of image parity as the six-dimensional parameter space is searched. Although computationally more expensive than the more popular simplex method[§] based optimization algorithms, it is significantly less prone to getting trapped in local optima.

[§] Descriptions of both simulated annealing and simplex methods in optimization routines are to be found in Press et al. (1992)

4 RESULTS AND A DISCUSSION OF THE LENS MODEL

The source positions, as found for the best-fit ($\phi = 9.83$ with a target σ of 5 mas) lens model are displayed in Table 2, and are plotted in Figure 1(b). Note particularly the success of the model in recovering the lobe double's source to lie just outside the cusp of the tangential critical curve, as mentioned in Section 2. The model image magnifications are also given in Table 2. The parameters of the best-fit model are given below; the errors quoted in brackets alongside are 90% confidence intervals from a Monte Carlo exercise. For this, the image positions have been subjected to random deviations, the magnitudes of which follow a normal probability distribution with a standard deviation of 5 mas from their nominal values. In the present case, 10000 such image configurations were sampled and put through the modeling process described above, with all six lens parameters free to vary. This took a total of 65 hours cpu time on a Sparc Ultra 1 machine. While 10^4 trials may seem a sparse sampling of the possible configuration space of random deviations in all the image positions put together, in practice the estimated confidence intervals alter only marginally between experiments with 10^4 trials and half that number (though a significant change occurs between 500 and 5000 trials).

The best-fit model obtained by the methods described in the previous sections yields lens parameters as below (with 90% confidence intervals quoted alongside):

Scale Length a : 113 mas (59, 224)mas
 Eccentricity e : 0.81 (0.73, 0.84)
 Mass Parameter σ_m : 79.8 (78.2, 84.1) km/s
 P.A. of Lens Major Axis: -46.5° (-47.0° , -46.1°)
 Lens Centre (RA, Dec. wrt cpt. 4): (423_{-5}^{+9} , 270_{-5}^{+7}) mas

Histograms of the distributions of the mismatch function ϕ and the various lens parameters, as obtained from the Monte Carlo exercise, are presented in Figure 2. The 'shoulder' in the plot for the mismatch function seen around the values of 12 to 13 is probably related to a similar feature seen in the plot for the position angle around -46.4 to -46.3 degrees, which is likely to be a consequence of the image parity constraints (sudden discontinuities result when a change of parameters places an image in a region of image space with the wrong parity).

The circular velocity $V_c(R)$ in the equatorial plane of the oblate spheroidal lens galaxy with mass density distribution as in Eqn.(1), can be estimated as a function of radial coordinate R from expression (2-91) in Binney & Tremaine (1987).

$$V_c^2(R) = 9\sigma_m^2 \frac{\sqrt{1-e^2}}{e} \frac{D_s}{D_{ls}} \left\{ \frac{\pi}{2} - \tan^{-1} \frac{\sqrt{1-e^2}}{e} - \frac{1}{\sqrt{1+R^2/(ae)^2}} \cos^{-1} \left(\frac{\sqrt{1-e^2}}{\sqrt{1+(R/a)^2}} \right) \right\} \quad (4)$$

In the limit of $e \rightarrow 0$, the right hand side of Eqn.(4) reduces to $9\sigma_m^2 (D_s/D_{ls}) \{1 - (a/R) \tan^{-1}(R/a)\}$. Asymptotically, the right hand side of Eqn.(4) is: $9\sigma_m^2 (\sqrt{1-e^2}/e) (D_s/D_{ls}) \{\pi/2 - \tan^{-1}(\sqrt{1-e^2}/e)\}$. From the above, it is seen that the circular velocity at a radius of $1''$ from the lens centre is $183\sqrt{D_s/D_{ls}}$ km/s, which, as R

tends to large values, achieves a maximum of $198\sqrt{D_s/D_{ls}}$ km/s.

The eccentricity e translates to a flattening or b/a ratio in the lens plane of $0.59_{-0.05}^{+0.09}$. This is marginally rounder than the value of $0.45 - 0.55$ suggested by the light profile in the HST I-band image, which is not surprising if the degree of flattening of the non-luminous component of the lens galaxy is somewhat smaller than that of its disk. It is of interest that the orientation of the lensing galaxy (p.a. -40 ± 5 degrees) accords so well with that required by our lens model. This strongly suggests that B1933+503 is lensed in the main by an isolated disk system. From Table 2, a comparison of the image flux density ratios with the model magnification values shows that the model actually predicts quite reasonably the flux density ratio of components 7 and 5, and with a lesser degree of success, the somewhat less reliable flux density ratio $8/1a$. In the case of the core images, departures of the model magnification ratios from the observed flux density ratios are apparent; these are probably the result of rapid intrinsic variations in the core flux density, as discussed earlier.

5 PREDICTED TIME DELAYS FOR THE IMAGES

Time delays between the four images of the core of the radio triple source, which we believe to be variable, are calculated for the mass density profile in Eqn.(1) using the formulae of Cooke & Kantowski (1975). The time delay, $\Delta\tau$, for the arrival at the observer of light from an image relative to, say, the undeflected source, is the sum of the time delay due to differences in geometric path length between the deflected and undeflected rays, $\Delta\tau_g$, and that due to the apparent slowing of light by the gravitational potential of the lens, $\Delta\tau_p$. With the mass density profile in Eqn.(1),

$$\Delta\tau_g = \aleph \frac{1}{2c} \left(\frac{4G}{c^2} \right)^2 |\mathbf{I}(\mathbf{z}_i)|^2$$

$$\Delta\tau_p = \aleph 36 \frac{\sigma_m^2 a \sqrt{1-e^2}}{c^3} \text{Re} \left\{ \int_0^{b_i} \frac{(\mathbf{z}_i/a)(\sqrt{1+b^2}-1)}{b\sqrt{(\mathbf{z}_i/a)^2 - (be)^2}} db \right\}$$

In the above expression, the quantity b_i is the value $(x^2 + y^2/(1-e^2))/a^2$, where $x + iy = \mathbf{z}_i$, the location of image i relative to the lens centre in the image plane. $\aleph = (1+z_l)(D_l/F_d)$, which combination of angular diameter distances has dimensions L^1 and calls for additional input: the lens and source redshifts and a cosmological model to be adopted. The integral in the expression for $\Delta\tau_p$ is evaluated numerically. Table 3 summarizes the time delay results; for the sake of completeness the delays for images arising from the lobes of the source are also listed. These are of relevance if monitoring reveals relative motion between the core and the knots, as is seen in compact symmetric objects (see Sec. 7.1 ahead).

6 FITS WITH SUBSETS OF CONSTRAINTS

It is interesting to ask how the modeling behaves when only one set of images is used. As discussed in Section 3.1, the positions of the four core images provide by themselves a

total of 6 constraints, which is exactly equal to the number of model parameters. Not surprisingly, an excellent match is obtained ($\phi_{CORE} = 0.421$), with the scale length restricted to be less than 10^{-5} asec (effectively a 5 parameter lens). The smallness of the mismatch function ϕ probably points to some degree of redundancy in the information provided by images in the core quad; the pairs 1 & 4 and 3 & 6 are fairly symmetrically disposed with respect to the lens major axis (Table 4). The image magnification ratios $3/1$, $4/1$ & $6/1$ are 0.95, 1.87 & 0.57 respectively. These should be compared with the observed values of 0.69, 2.61 & 0.61 for these images, recalling that they are known to be highly variable, and with the original model values of 1.13, 2.08 & 0.86 respectively. (The value of ϕ_{CORE} for the core images alone in the original model is 3.9 and for all the images together is $\phi_{ALL} = 9.8$). However, if the scale length is restricted and modeling is undertaken of all the images together, the fit is a bit worse: $\phi_{ALL} = 15.9$ for all the images together, or $\phi_{CORE} = 10.3$ for the core images alone. Save for the scale length in these various models, the other parameters are similar; the lens centre shifts by between 10 to 20 mas between models, and the model velocity dispersion and eccentricity change by about 4%, which is within the 90% confidence limits on the original model. The orientation angle is almost unaffected. VLBA and MERLIN observations underway (Sykes et al. 1997) should provide better determined constraints from which to build more accurate models in the future.

7 DISCUSSION AND CONCLUSIONS

Is B1933+503 a lensed system? Despite the absence of optical information on the images and a redshift for the source, the simplicity with which the lensing picture explains this strikingly unusual ten component system indicates that it is not just a collection of physically related radio features but is indeed a lensed source. This conclusion is underlined by the fact that actual lens modeling accounts so well for details of the observations.

The Mass Profile of the Lens Galaxy: The mass model adopted (a non-singular isothermal ellipsoid) is only an approximation to possibly more complex substructure within the lens, especially if it is a disk system as is suggested by the high degree of flattening in the optical image. Since three source components are lensed by the same galaxy, it will provide a strong test of the usual simplifying assumptions made when modeling lensed systems. Although a quad system provides a surfeit of constraints (6 positional + 3 image flux ratio = 9) over parameters for a simple 6 parameter lens model such as the one used in the present work, the images typically tend to form at roughly the same radial distance from the centre of the lens and convey little information on the radial profile or the scale length the mass distribution of the galaxy. This is particularly true if the the scale length is quite small compared with the scale of the image splitting. A double image system manages to sample radially distinct portions of the lens, but in general on its own does not provide enough constraints (2 positional + 1 image flux ratio = 3 quantities) for even the simplest elliptical lens models. B1933+503 is remarkable in having two quads *and* a double, and the fact that the best-fit model calls for a non-singular

lens model (scale length of 113 mas, translating to a typical value of about 0.5 kpc at $z_l = 0.755$, $H_o = 100$ km/s/Mpc) is therefore a matter of some significance.

Predictions for high-resolution observations: The constraints used in the present model are independent of the image flux density ratios, but modeling relies upon the image parities, which are robust constraints. The image parities are usually weak constraints in a quad or a double image system, but in the present 10-image configuration effectively restrict the location of the tangential critical curve. The model in this paper makes certain predictions: (i) Magnification ratios for the core images are given in Table 2, as obtained from modeling. Monitoring variations in the flux density these images will provide both the time delays (also predicted by the model, see Table 3) and the actual lens magnification ratios. (ii) The source of the quad (2a, 2b, 5, 7), a knot with a steep radio spectrum, should itself be multicomponent or extended. In the present model, this source is only partially imaged in the vicinity of 2a and 2b. VLBA observations at 1.7 GHz have been carried out (Marlow et al. 1997), and these should reveal with greater accuracy the correspondence between the peaks in 2a and 2b and features in the other images 5 and 7.

7.1 The source — a Compact Symmetric Object?

The source of this remarkable ten-image system appears to be a compact radio triple source, an almost linear set of knot, core and a second, weaker knot. The stronger and weaker knots have separations of 194.5 and 120 mas from the core in the present model (see Table 2). This corresponds to a physical extent of about 1.3 kpc ($H_o = 100$ km/s/Mpc) and thus the source could be a compact symmetric object (Readhead et al. 1994). Observations over time will indicate, by changes in the locations and/or image flux densities of the knot images, whether they are moving relative to the central core, as in the case of the radio galaxy 1946+708 (Taylor & Vermeulen 1997). While this would no doubt complicate the modeling described earlier, it would in itself be a very interesting phenomenon to observe. It will be necessary to ‘deconvolve’ the effects due to differences in light travel time to the observer for the different images from those due to the intrinsic source motion. Each epoch of observation will catch up to four *different* phases in the time evolution of the source structure in each quad, due to the relative time delays between the images. In addition, there is the advantage of spatial magnification due to lensing, which can be as high in specific directions as factors of 10–20 for images such as 2a, 2b, and 8. The model in the present paper makes an interesting prediction in the event that the brighter knot moves outward from the core (see Figure 1): the peaks of images 2a and 2b should disappear after initially brightening and then merging with each other. Image 5 will also move outward with respect to image 4. If the fainter knot moves outward from the core, image 8 should initially become fainter (it moves into a region of lower magnification); there will be an increase in separation between images 1 and 1a.

7.2 B1933+503 as a cosmological probe

A well-established goal of gravitational lensing is to determine values of parameters for cosmological models (Refsdal

1964). From the expressions in Section 5, the factor N is inversely proportional to Hubble’s Constant; thus, with a well-fit model for the lens and measured values for the time delays between pairs of images, it is possible to estimate Hubble’s Constant within a specific cosmological model. However, the quantity N involves the source redshift, z_s , which in the case of B1933+503 is unknown. A study of the lens galaxy could provide the key to using this system to estimate Hubble’s Constant. From Section 5, it is evident that information involving the source redshift is restricted to the term F_d . If it proves possible to observationally determine the circular velocity V_c of the lens through redshifted HI or molecular line studies, then from Equation (4) and the model parameters, the quantity $F_d = D_s/D_{ls}$ is obtainable in principle. This is under the assumption that lensing is due to the galaxy at $z_l = 0.755$, with no significant contribution from external shear or matter along the line of sight. In view of the degree to which the simple model presented here accounts for B1933+503, this does not seem unreasonable. In general, the presence of distributed matter along the line of sight cannot be ruled out, so at least an upper bound can be put on the value of Hubble’s Constant.

The treatment in this paper assumes that the lens is viewed edge-on; including an inclination along the line of sight is straightforward with regard to the lens model (see Bourassa & Kantowski 1975), and should observations provide sufficient detail to permit the inclination to be established, B1933+503 will be a rather promising system for cosmological studies.

ACKNOWLEDGMENTS

The author gratefully acknowledges discussions with Ian Browne and Chris Sykes, with Roger Blandford regarding the lens modeling, Dan Marlow and Peter Wilkinson regarding the VLBA observations, with Neal Jackson regarding the HST observations of the lens, and with Rene Vermeulen regarding the nature of the source. Bill Goffe kindly provided details of his optimization code. Many discussions with Leon Koopmans made the work both stimulating and a pleasure, and the author is grateful to Ger de Bruyn for discussions about future observational possibilities with B1933+503. The Astronomical Institute ‘Anton Pannekoek’, University of Amsterdam and the Netherlands Foundation for Research in Astronomy, Dwingeloo, are gratefully acknowledged for the use of their computing facilities, as is the pulsar group at Jodrell Bank, on whose computers the initial simulations were run. The author acknowledges NWO grant number B-78-344 while in the Netherlands.

REFERENCES

- Augusto, P. et al., 1996, in *Astrophysical Applications of Gravitational Lensing*, eds. Kochanek, C.S & Hewitt, J. N. (Dordrecht: Kluwer)
- Binney, J. & Tremaine, S. 1987, *Galactic Dynamics*, Princeton University Press, Princeton, N.J., USA
- Blandford, R.D. & Narayan, R. 1986, *ApJ*, 310, 568
- Bourassa, R.R., Kantowski, R. & Norton, T.D., 1973, *ApJ*, 185, 747
- Bourassa, R.R. & Kantowski, R., 1975, *ApJ*, 195, 13

- Browne, I.W.A. et al., 1997, in ‘Observational Cosmology with the new radio surveys’, eds. Bremer, M., Jackson, N. & Perez-Fournon, I. (Kluwer)
- Cooke, J.H. & Kantowski, R., 1975, ApJ, 195, L11
- Fassnacht, C.D., Womble, D.S., Neugebauer, G., Browne, I.W.A., Readhead, A.C.S, Matthews, K & Pearson, T.J, 1996, ApJ, 467, 73
- Goffe, W.L., Ferrier, G.D. & Rogers, J. 1994, J. Econometrics, 60, 65
- Jackson, N., et al., 1995, MNRAS, 274, L25
- Jackson, N., et al., 1997a, MNRAS, in press
- Jackson, N., Nair, S. & Browne, I.W.A., 1997b, in ‘Observational Cosmology with the New Radio Surveys’, eds. Bremer, M., Jackson, N. & Perez-Fournon, I. (Kluwer)
- Kassiola, A. & Kovner, I. 1993, ApJ, 417, 450
- Kayser, R. & Schramm, T. 1988, A&A, 191, 39
- King, L.J. & Browne, I.W.A. 1996, MNRAS, 282, 67
- King, L.J., Browne, I.W.A., Muxlow, T.W.B., Narasimha, D., Patnaik, A. R., Porcas, R.W. & Wilkinson, P.N., 1997a, MNRAS, 289, 450
- King, L.J., Jackson, N.J., Blandford, R.D., Bremer, M.N., Browne, I.W.A., de Bruyn, A.G., Fassnacht, C., Koopmans, L., Marlow, D., Nair, S. & Wilkinson, P.N., 1997b, submitted
- Kochanek, C.S. 1991, ApJ, 373, 354
- Koopmans, L., de Bruyn, A.G. & Jackson, N., 1997a, MNRAS, submitted
- Koopmans, L. et al., 1997b, in preparation
- Marlow, D. et al., 1997, in preparation
- Myers, S., et al., 1995, ApJ, 447, L5
- Patnaik, A.R., Browne, I.W.A., Walsh, D., Chaffee, F.H. & Foltz, C.B., 1992, MNRAS, 259, 1P
- Patnaik, A. R., Browne, I.W.A., King, L.J., Muxlow, T.W.B., Walsh, D. & Wilkinson, P.N., 1993, MNRAS, 261, 435
- Press, W.H., Teukolsky, S.A., Vetterling, W.T. & Flannery, B.P. 1992, *Numerical Recipes in Fortran: The Art of Scientific Computing*, Cambridge Univ. Press, Cambridge, Mass., USA
- Rao, A. Pramesh & Subrahmanyam, R., 1988, MNRAS, 231, 229
- Readhead, A.C.S., Taylor, G.B., Xu, W., Pearson, T.J., Wilkinson, P.N. & Polatidis, A.G., 1994, ApJ, 460, 612
- Refsdal, S., 1964, MNRAS, 128, 307
- Schneider, P., Ehlers, J. & Falco, E.E., 1992, *Gravitational Lenses* (New York: Springer)
- Sykes, C.M. et al., 1997, companion paper, astro-ph/9710358
- Taylor, G.B. & Vermeulen, R.C., 1997, ApJ, 485L
- Xanthopoulos, E. et al., 1997, in preparation

This paper has been produced using the Royal Astronomical Society/Blackwell Science L^AT_EX style file.

Image	Rel. (RA, Dec) (mas)	Obs. flux ratio at Freq. (GHz)			
		1.7	5	8.4	15
2a	(171, 414)	...			
2b	(51, 420)	...			
5	(-531, -497)	1.00	1.00	1.00	1.00
7	(398, -134)	1.25	1.15	1.16	1.13
1	(447, 495)	1.00	1.00	1.00	1.00
3	(-389, 158)	0.69	0.84	0.79	0.61
4	(-397, -299)	2.61	3.46	3.65	3.78
6	(230, -387)	0.61	0.96	0.83	0.78
1a	(545, 584)	1.00			
8	(-114, -335)	4.00			

Table 1. Inputs to the modeling: For each set of images, the positions relative to an initial guess lens centre at (397,299) mas wrt image 4, and the image flux ratios relative to that image of each set whose value is 1.00, for various frequencies of observation. The model uses only the 1.7 GHz data; the other observations are included in the Table to indicate the (un)reliability of various image flux ratios as constraints. Values for images 2a & 2b are not listed as it is apparent that these are mappings of only a fraction of the source of images 5 & 7 (see text). In the higher frequency observations, the resolution and/or dynamic range was inadequate to pick up 2a & 2b as separate components. Images 1a & 8 are not detected in the higher frequency observations. The core images 1, 3, 4 & 6 show signs of variability (*cf.* discussion in Sykes et al. 1997). Most data are derived from Sykes et al. (1997); positions for 2a & 2b are from Browne (private communication).

Image Set	Model Magn.	Flux Ratio (obsvd)	P_m (P_{em})	Source Pos. (mas)
Lobe quad:				
5	2.58	1.00	+1	$\delta RA :$
		1.00	+1	-105 ± 5
7	3.05	1.18 (1.03, 1.62)	-1	$\delta Dec :$
		1.25 (± 0.04)	-1	-66 ± 1
2a	+1	
			+1	
2b	-1	
			-1	
Core quad:				
1	2.89	1.00	+1	$\delta RA :$
		1.00	+1	36 ± 3
3	3.25	1.13 (1.02, 1.42)	-1	$\delta Dec :$
		0.69 (± 0.14)	-1	68 ± 4
4	6.01	2.08 (1.98, 2.52)	+1	
		2.61 (± 0.31)	+1	
6	2.48	0.86 (0.75, 1.16)	-1	
		0.61 (± 0.13)	-1	
Lobe double:				
1a	2.28	1.00	+1	$\delta RA :$
		1.00	+1	123 ± 5
8	14.24	6.24 (4.62, 10.22)	-1	$\delta Dec :$
		4.00 (± 1.83)	-1	151 ± 4

Table 2. Model Predictions: For the components grouped as discussed in Section 3, the model magnifications, model flux density ratios (with 90% confidence intervals determined from a Monte Carlo exercise alongside) — in the succeeding line, these are compared with observed values taken from the 1.7 GHz map of Sykes et al. 1997 (with errors as inferred from that paper); the model image parities P_m (with the theoretically expected values P_{em} on the following line), and the model-recovered source positions ($\delta(RA)$, $\delta(Dec)$) for each image group, w.r.t the lens centre. The source positions are mean values for all backprojected images belonging to a particular group (i.e., quad or double). Beside these values are the standard deviations for each set, for the best-fit model itself; ideally, these should be as small as possible.

Image Set	Time Delay (in units \aleph days/Gpc)	90% Confidence Interval
Lobe quad:		
5	0.00	...
7	4.32	(3.56, 4.89)
2a	3.66	(3.14, 4.05)
2b	3.83	(3.20, 4.29)
Core quad:		
1	0.00	...
3	2.74	(2.11, 3.13)
4	2.37	(1.95, 2.71)
6	3.15	(2.52, 3.58)
Lobe Double:		
1a	0.00	...
8	6.22	(5.15, 7.02)

Table 3. Predicted time delays for the three image sets: The image listed at top in each set is the reference image corresponding to the global minimum in arrival times for light from the source (core or a lobe). $\aleph = (1 + z_l)(D_l/F_d)$, as discussed in Section 5 (see text); a typical value is 3 Gpc). The last column lists the 90% confidence intervals for each value, from the Monte Carlo exercise.

Image Set	B value (asec)	$ \psi $ (degrees)
Lobe Quad:		
5	1.24	83
7	0.46	27
2a	0.75	65
2b	0.66	51
Core Quad:		
1	1.14	86
3	0.50	19
4	0.80	75
6	0.44	17
Lobe Double:		
1a	0.80	3
8	0.37	19

Table 4. Illustrating the extent of sampling of the lens plane by the various image systems. B is the elliptical radius of the given image: in Cartesian coordinates, referred to the lens centre and with the x -axis along the lens major axis, $B^2 = x^2 + y^2/(1 - e^2)$. $|\psi|$, the norm of the angle each image makes with respect to the lens major axis (when referred to the lens centre), is listed alongside. Images of similar $|\psi|$ and B values provide similar constraints on the modeling if they belong to the same image system.

Figure 1. Lens model for B1933+503. (a) : Image plane critical curves for the lens model, on which observed image positions have been superposed. The lens is centred at (0,0). Images landing very near a critical curve suffer very high magnifications, tending to merge with nearby images across such curves (2a with 2b, for example). Image positions marked by open circles with central dots form the quad arising from lensing of the source's core, open circles mark one lobe's quad images, and the small filled squares denote the other lobe's double images. (b) : The corresponding source plane caustics for the model. The positions of the three source components are marked with symbols corresponding to their images, a circle with a dot for the core of the source, an open circle for the stronger lobe and a small filled square for the weaker one. The cross superposed on the open circle is the source location when the positions of images 2a and 2b are included (see Section 3.1); the slight offset with respect to the original source position, obtained from images 5 and 7 alone, arises because images 2a and 2b represent only a fraction of the source that gets mapped onto 5 and 7.

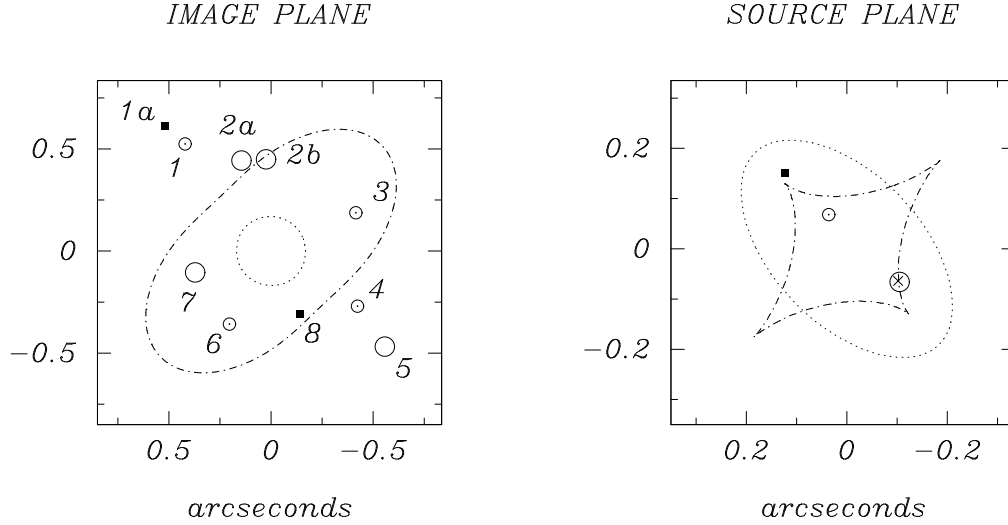


Figure 2. Results from the Monte Carlo exercise (Section 4). The plots are histograms of binned values of the six lens parameters, and of the mismatch function ϕ . The plot for the mismatch function shows the buildup of the distribution as the number of experiments, N_{exp} , is increased from 10^3 to 10^4 . Note that the lens parameters are varied *simultaneously* in this set of experiments, which results in a significantly wider spread in recovered values than is currently recognised in the literature. A spread of the order of 30 % is apparent in the predicted time delay values as well (Table 3).

